TIME DOMAIN FULL WAVEFORM INVERSION USING A TIME-WINDOW AND HUBER FUNCTION NORM

MINKYUNG SON[1], YOUNGSEO KIM[2], CHANGSOO SHIN[3] and DONG-JOO MIN[3]

[1] *Earthquake Research Center, Korea Institute of Geoscience and Mineral Resources, Seoul, South Korea.*
[2] *Department of Energy System Engineering, Seoul National University, Seoul, South Korea.*
[3] *Research Institute of Energy and Resources, Seoul National University, Seoul, South Korea.*
css@model.snu.ac.kr

(Received October 8, 2012; revised version accepted July 10, 2013)

ABSTRACT

Son, M., Kim, Y., Shin, C. and Min, D.-J., 2013. Time domain full waveform inversion using a time-window and Huber function norm. *Journal of Seismic Exploration*, 22: 311-338.

To prevent the solution of full waveform inversion from converging to the local minimum, we present a full waveform inversion method with a data selection strategy using time-windows in the time domain. Adopting ideas from previous studies to mitigate the problem of local minima in the frequency domain full waveform inversion, we define the time-window to be associated with the highest amplitude of each observed trace. The time-window makes its corresponding data to be given greater weight in the calculation of the objective function. We apply also the Huber norm composed of a combination of l^1 and l^2 norms and use the approximated Hessian matrix both of which have been used in the frequency domain. The proposed algorithm is validated with two synthetic datasets and one real dataset. These include data from the simple anticline model, low-pass filtered data from the IFP Marmousi model, and data acquired from the Gulf of Mexico. We demonstrate that the inverted velocity models from the two synthetic datasets are in good agreement with the true models. In the real data example a reasonable velocity model is obtained which improves the reverse-time migration images.

KEY WORDS: full waveform inversion, acoustic wave equation, local minimum, time-window, Huber norm.

INTRODUCTION

Since Tarantola (1984) suggested that the back-propagation method was capable of constructing the gradient (or steepest descent) direction without explicitly computing the partial derivatives in the time domain, full waveform inversion has been used as a tool to estimate subsurface information such as velocity, density or impedance. However, the practical applications of full waveform inversion have been limited because of the existence of many local

0963-0651/13/$5.00

minima in the calculation of an objective function, which hinders the solution from converging to the global minimum. In frequency domain waveform inversion, many studies have been conducted to solve this problem. Sirgue and Pratt (2004) used the results of refraction tomography as an initial velocity model in the waveform inversion. Kim et al. (2010) reduced the number of local minima by removing some of the forward wavefields, which make the partial derivative wavefields unstable. Ha et al. (2009) used the Huber norm constructed by the combination of the l^1 and l^2 norms as an objective function.

Adopting these ideas to time domain waveform inversion, we suggest using a time-window similar to the filtering technique suggested by Kim et al. (2010) and employing the Huber norm as an objective function. Based on the idea of depth-staging technique proposed by Varela et al. (1998), we divide the inversion process into several stages with a time-window. Our time-window includes the time corresponding to the highest amplitude of each observed trace in each stage. The values of the observed and modeled data located in the time-window comprise a residual vector. This residual is for computing the objective function to obtain an inverted velocity model. After the objective function has decreased sufficiently, the data covered by the new time-window are employed again in an iterative inversion process.

This paper is organized as follows: we review the Huber function norm with the conventional algorithm of the full waveform inversion in the time domain and estimation of source wavelet, and then explain the data selection strategy with time-windows in detail. Inverted velocity model of the simple anticline model and Institut Français du Pétrole (IFP) Marmousi (Bourgeois et al., 1991) are presented. We conclude by comparing the proposed algorithm with the conventional algorithm through inverted results of the real dataset from the Gulf of Mexico.

TIME DOMAIN FULL WAVEFORM INVERSION WITH THE HUBER FUNCTION

Here we review the methodology of the full waveform inversion in the time domain using the Huber function norm and the back-propagation algorithm. Huber (1973) suggested an objective function in the following form:

$$M_\varepsilon(r) = \begin{cases} |r|^2/2\varepsilon \ , & |r| \le \varepsilon \\ |r| - \varepsilon/2 \ , & |r| > \varepsilon \end{cases} \tag{1}$$

where ε is the threshold between the l^1 and l^2 errors for the real values of r. Following Ha et al. (2009), we use the threshold of Bube and Nemeth (2007).

Using a Huber function norm, the objective function can be defined in terms of a parameter vector, **p**, in the time domain as follows:

$$E(\mathbf{p}) = \sum_{i=1}^{N_s} \sum_{j=1}^{N_r} M_\varepsilon(r_{i,j}) \quad , \tag{2}$$

where $r_{i,j} = u_{i,j} - d_{i,j}$, $u_{i,j}$ and $d_{i,j}$ are the modeled and observed pressure wavefields at the i-th receiver and j-th shot, respectively, N_s is the number of sources, and N_r is the number of receivers.

To minimize the objective function, the gradient is calculated by taking the partial derivative of the objective function with respect to the k-th model parameter, p_k, as follows:

$$\begin{cases} \partial E/\partial p_k = \sum_{i,j} (\partial u_{i,j}/\partial p_k)(1/\varepsilon)(u_{i,j} - d_{i,j}) \quad , & \text{if } |r_{i,j}| \le \varepsilon \\ \partial E/\partial p_k = \sum_{i,j} (\partial u_{i,j}/\partial p_k)\mathrm{sgn}(u_{i,j} - d_{i,j}) \quad , & \text{if } |r_{i,j}| > \varepsilon \end{cases} \tag{3}$$

when if $|r_{i,j}| > \varepsilon$ the sign function is

$$\mathrm{sgn}(a) = \begin{cases} 1, & \text{if } a > 0 \\ -1, & \text{if } a > 0 \\ 1, & \text{if } a > 0 \end{cases} . \tag{4}$$

To obtain the partial derivative wavefield of eq. (3), we use a gradient of the objective function in the frequency domain, in which we can express convolutions more simply than in the time domain. The gradient with a back-propagation algorithm in the frequency domain is defined as:

$$\partial E/\partial p_k = \sum_{i=1}^{N_s} \int_0^{\omega_{max}} \mathrm{Re}[(\tilde{\mathbf{f}}_{v,i})^T (\tilde{\mathbf{S}}^T)^{-1} \tilde{\mathbf{r}}_i^*] d\omega \quad , \tag{5}$$

where ω is the angular frequency, $\tilde{\mathbf{f}}_v$ is the virtual source vector (Shin and Min, 2006), $\tilde{\mathbf{r}}$ is a residual pressure wavefield, * denotes a complex conjugate, and T is a transpose operator.

The combination of the second and third terms $(\tilde{\mathbf{S}}^T)^{-1}\tilde{\mathbf{r}}_i^*$ in eq. (5) represents the back-propagation of the residuals. Thus, this conjugate residual wave propagates backward through the medium, which is denoted by the back-propagated wavefields of the time domain, **B**(t). Because multiplication in the frequency domain is equivalent to convolution in the time domain, gradient direction is expressed with back-propagated wavefield **B** as follows:

$$\partial E/\partial p_k = \sum_{i=1}^{N_s} \int_0^{T_{max}} \mathrm{Re}[(\mathbf{f}_v^i)^T[\mathbf{B}(T_{max} - t)]dt \quad , \tag{6}$$

where T_{max} is the maximum record length, and $\mathbf{f}_v^i$ is the virtual source for the i-th shot.

The virtual source vector is shown in eq. (7), where n is the number of parameters.

$$\mathbf{f}_v = [f_{v,1}(t) \cdots f_{v,k}(t) \cdots f_{v,n}(t)]^T \quad . \tag{7}$$

The virtual source is obtained by taking the partial derivative of the waveform equation. The acoustic waveform equation is as follows:

$$(1/p^2)(\partial^2 u/\partial t^2) = (\partial^2 u/\partial x^2) + (\partial^2 u/\partial y^2) + f(x,y,t) \quad , \tag{8}$$

with

$$f(x,y,t) = \delta(x - x_s)\delta(y - y_s)w(t) \quad , \tag{9}$$

where p is the model parameter, u is the pressure wavefield, δ is the delta function, x_s and y_s are the source points of the shot in x- and y-directions, respectively, and w is a source wavelet.

Eq. (10) below is derived by taking the partial derivative of Eq. (8) with respect to the model parameter p. We arrange eq. (10) to the form of wave equation, eq. (8) as follows:

$$-(2/p^3)(\partial^2 u/\partial t^2) + (1/p^2)(\partial^2/\partial t^2)(\partial u/\partial p)$$

$$= (\partial^2/\partial x^2)(\partial u/\partial p) + (\partial^2/\partial y^2)(\partial u/\partial p) \quad , \tag{10}$$

$$(1/p^2)(\partial^2/\partial t^2)(\partial u/\partial p) = (\partial^2/\partial x^2)(\partial u/\partial p)$$

$$+ (\partial^2/\partial y^2)(\partial u/\partial p) + (2/p^3)(\partial^2 u/\partial t^2) \quad . \tag{11}$$

Let the partial derivative of wavefield $\partial u/\partial p$ be J. We can consider eq. (11) to be an acoustic wave equation with a source f_v, as shown in eq. (12).

$$(1/p^2)(\partial^2 J/\partial t^2) = (\partial^2 J/\partial x^2) + (\partial^2 J/\partial y^2) = f_v \quad , \tag{12}$$

$$f_v = (2/p^3)(\partial^2 u/\partial t^2) \quad . \tag{13}$$

In the proposed algorithm, a source $f_{v,k}$, which is the virtual source for the k-th model parameter, is defined as follows:

$$f_v = (2/p_k^3)(\partial^2 u/\partial t^2)_k \approx (2/p_k^3)[(u_k^{it-1} - 2u_k^{it} + u_k^{it+1})/\Delta t^2] \quad . \tag{14}$$

In the course of modeling, we have the wavefield of the current time-step it, the previous time-step it − 1 and the next time-step it + 1, with a time interval Δt. The k-th partial derivative of wavefield $(\partial^2 u/\partial t^2)_k$ of eq. (14) is computed via the second order finite difference method.

For the solution to converge to the global minimum, the gradient direction of eq. (6) is scaled by the diagonal of the approximated Hessian introduced by Shin et al. (2001). Finally, we obtain eq. (15) updating the model parameter $\mathbf{p}$,

$$\mathbf{p}^{iter+1} = \mathbf{p}^{iter} + \alpha \cdot NRM\left[\sum_{i=1}^{N_s}\left[\int_0^{T_{max}}\{[\mathbf{f}_{v,i}^T \mathbf{B}(T_{max} - t)dt]/\left[\int_0^{T_{max}} \mathbf{f}_{v,i}^T \mathbf{f}_{v,i} dt + \gamma\right]\}\right]\right], \quad (15)$$

where iter represents the iter-th iteration, α is the step length, which is equivalent to a grid interval, NRM is the normalization suggested by Ha et al. (2009), δ is the damping constant added to avoid the singularity of the proposed Hessian matrix, and is set equal to 0.1% of the maximum value of the approximated Hessian matrix's diagonal.

SOURCE ESTIMATION

The source wavelet, which is the input signal acting as one of the important factors for simulating wavefield, should be estimated before modeling the forward data. According to Kim et al. (2011), a source wavelet has been assumed to be a near-offset trace (Vigh and Starr, 2008) or a well-known synthetic function, such as a Ricker wavelet or the first derivative of a Gaussian function. To acquire more reliable inversion results, Song et al. (1995) suggested an inversion for the source wavelet instead of the physical properties of a target. Pratt (1999) and Shin and Min (2006) validated that the source estimation allows better results to be obtained. We depict the flow of full waveform inversion with source estimation in Fig. 1. Two approaches for source estimation are used: the first approach is the Green's functions via an additional forward modeling, and the other approach is scaling the relative amplitudes between the observed and forward-modeled data.

Employment of the Green's functions

We estimate a source wavelet in the frequency domain following Shin et al. (2007), and then transform the source wavelet to the time domain. The source wavelet in the frequency domain, e+if can be expressed as eq. (23), where the observed data at the j-th receiver is a+ib, the Green's function for the true velocity model is c+id and i is $\sqrt{-1}$.

$$e_j + if_j = [\sum_j (a_j c_j + b_j d_j) / \sum_j (c_j^2 + d_j^2)] - i[\sum_j (a_j d_j + b_j c_j) / \sum_j (c_j^2 + d_j^2)] = \sum_j (a_j + ib_j)(c_j + id_j)^* / \sum_j (c_j + id_j)(c_j + id_j)^* \quad . \quad (16)$$

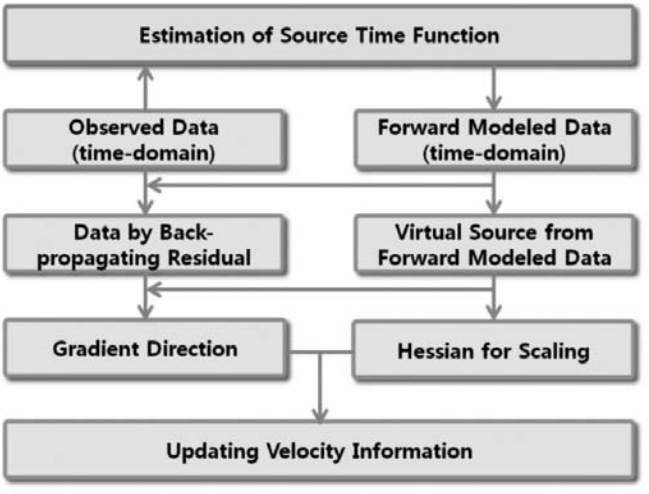

Fig. 1. Flow of the full waveform inversion with source estimation.

The Green's function for the true velocity model in eq. (16) is replaced by the Green's function for the inverted velocity model at each iterative step of the full waveform inversion. As shown in Fig. 2 the source wavelet in the frequency domain is estimated, after the observed data transformed from the time domain is divided by the Green's function for the inverted velocity model. The Green's function for the inverted velocity model in the frequency domain is equal to an arbitrary wavelet over the forward modeled data generated from the arbitrary wavelet. The Gaussian function is employed as the arbitrary source wavelet, and has the maximum frequency adequate to the condition for the modeling in the time domain. The frequency domain data including the arbitrary wavelet and the forward modeled data are transformed from the time domain data via an additional forward modeling. In Fig. 2, 'FT' and 'IFT' represent 'Fourier Transform' and 'Inverse Fourier Transform', respectively.

To mitigate ringing effects resulting from the imperfect deconvolutions, we applied a moving average and tapering to the recovered source wavelet. The moving average was also applied to all of the time indices of the recovered source wavelet, and tapering with cosine functions was used near the both starting and ending time of source wavelet.

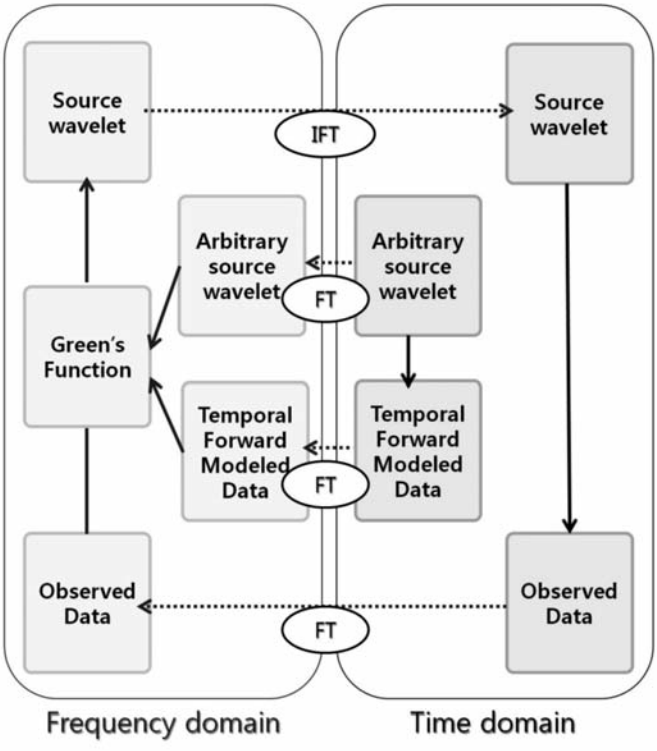

Fig. 2. Algorithm of the source estimation in the time and frequency domain.

Relative amplitude scaling

We scale the amplitudes of the observed data to those of the forward-modeled data because the observed and forward-modeled data establish the residual, which is one of the critical factors in full waveform inversion. However, the residual is biased toward either observed or forward-modeled data if the amplitudes of one of the data have absolute values much larger than those of the other data's amplitudes.

To prevent the residual from being biased, the amplitudes of the observed data to those of the forward-modeled data for the i-th shot is scaled as follows:

$$\bar{\mathbf{d}}_i = \mathbf{d}_i\{\mathrm{Max}[\mathbf{u}_i]/\mathrm{Max}[\mathbf{d}_i]\} \quad , \tag{17}$$

where $\bar{\mathbf{d}}_i$ is the scaled observed data, and $\mathbf{u}_i$ and $\mathbf{d}_i$ are the forward-modeled data and observed data, respectively. The forward-modeled data is generated from a known source wavelet. We employ the first derivative of the Gaussian function as a known source wavelet in the proposed algorithm.

The residual for the i-th shot, thus, is presented as follows:

$$\mathbf{r}_i = \mathbf{u}_i - \bar{\mathbf{d}}_i \quad . \tag{18}$$

The residual in eq. (18) is used to compute the back-propagated wavefield, which is employed to obtain the gradient direction, as shown in eq. (18).

Data selection with a time-window

We propose a full waveform inversion with a time-window for data selection to make the steepest descent be directed toward the global minimum. To determine the time-window, we select a reference time for each trace. Assuming that T_{top} represents the time corresponding to the highest amplitude of an observed trace, we can set up a time-window that ranges from T_{w-min} to T_{w-max} as follows:

$$\begin{aligned} T_{w-min} &= T_{top} - q \times N_t \quad , \\ T_{w-max} &= T_{top} + q \times N_t \quad , \\ N_t &= T_{max}/\Delta t + 1 \quad , \end{aligned} \tag{19}$$

where T_{max} is the total recording time, Δt is a sampling interval, and q is a real number smaller than 1, and is constant through the entire process. Time-window concept is depicted by the blue area in Fig. 3(a). We apply the time-window to the seismogram of Fig. 3(b), generated from the IFP Marmousi model with the first derivative of the Gaussian function.

Instead of setting up a new time-window for the forward trace, the time-window made from an observed trace is applied to the forward trace, which has the same position as an observed trace. The observed and modeled wavefields not located on the interval between T_{w-min} and T_{w-max} are set to zero as shown in Fig. 4(a), and excluded from the calculation of the residuals used to obtain the gradient. The velocity is inverted by the gradient, and the objective function that was computed from the difference between the observed and modeled data converges. This convergence marks the end of the first stage of inversion with the proposed algorithm.

As shown Fig. 5(a), we find a new reference time T_{top} corresponding to the highest amplitude of the observed data remaining after the first filter. Using the new reference time, we set up a new time-window. The seismogram after the second time-windowing is shown in Fig. 5(b). The inversion begins again using the velocity model inverted from the previous stage as an initial velocity model. In this manner, the velocity could be updated by adding new information.

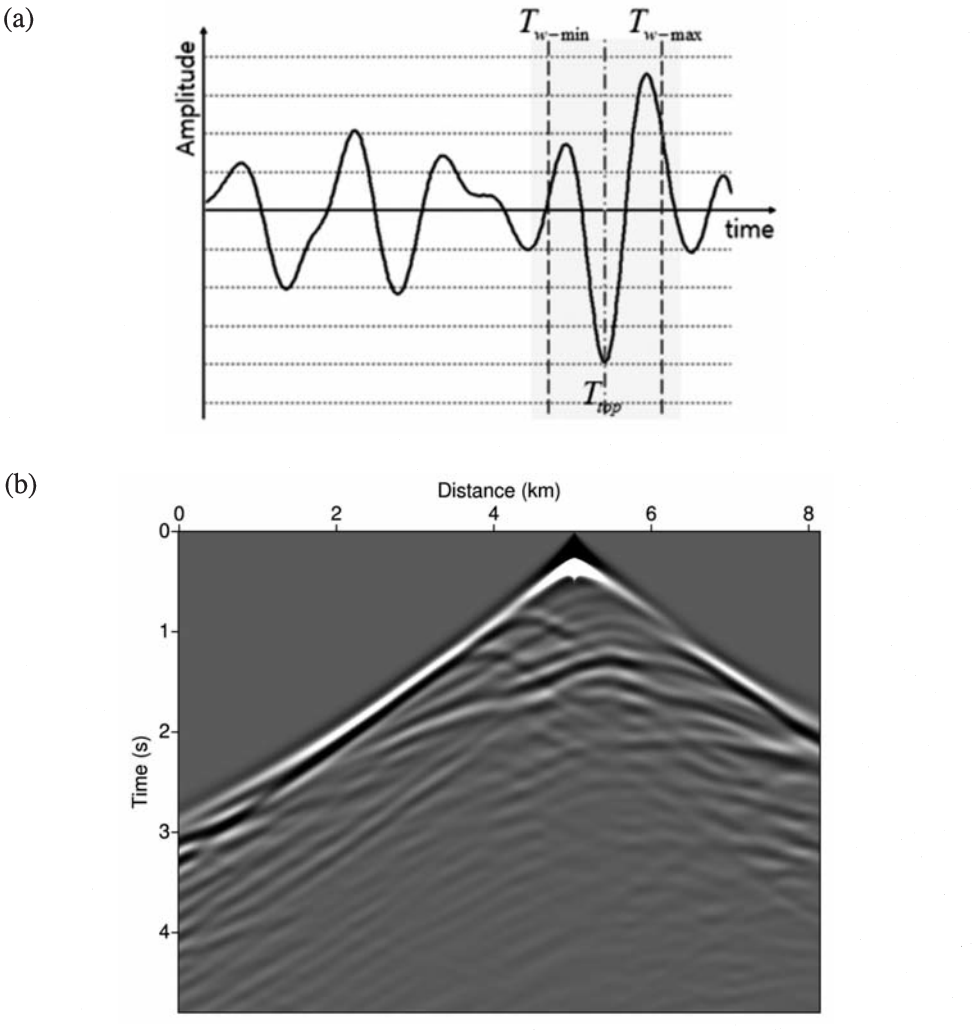

Fig. 3. (a) Time-window concept (blue area); (b) seismogram to be tested by the time-windows.

Fig. 6 shows the flow for the waveform inversion using time-windows; the flow consists of two loops: one for the iteration and one for the stages. For example, the first stage of the proposed process is the full waveform inversion with n_{iter} iterations for the data included by the first time-window. In Fig. 6, n_{stage} is defined to be larger than the reciprocal of p, or the record time over the length of time-window because when strong amplitudes are crowded, a secondary time-window may partly overlap with the time-window established in the previous stages. By increasing the value of n_{stage}, we can avoid omitting data in the course of the selection by time-windows and sufficiently utilize the large-amplitude data.

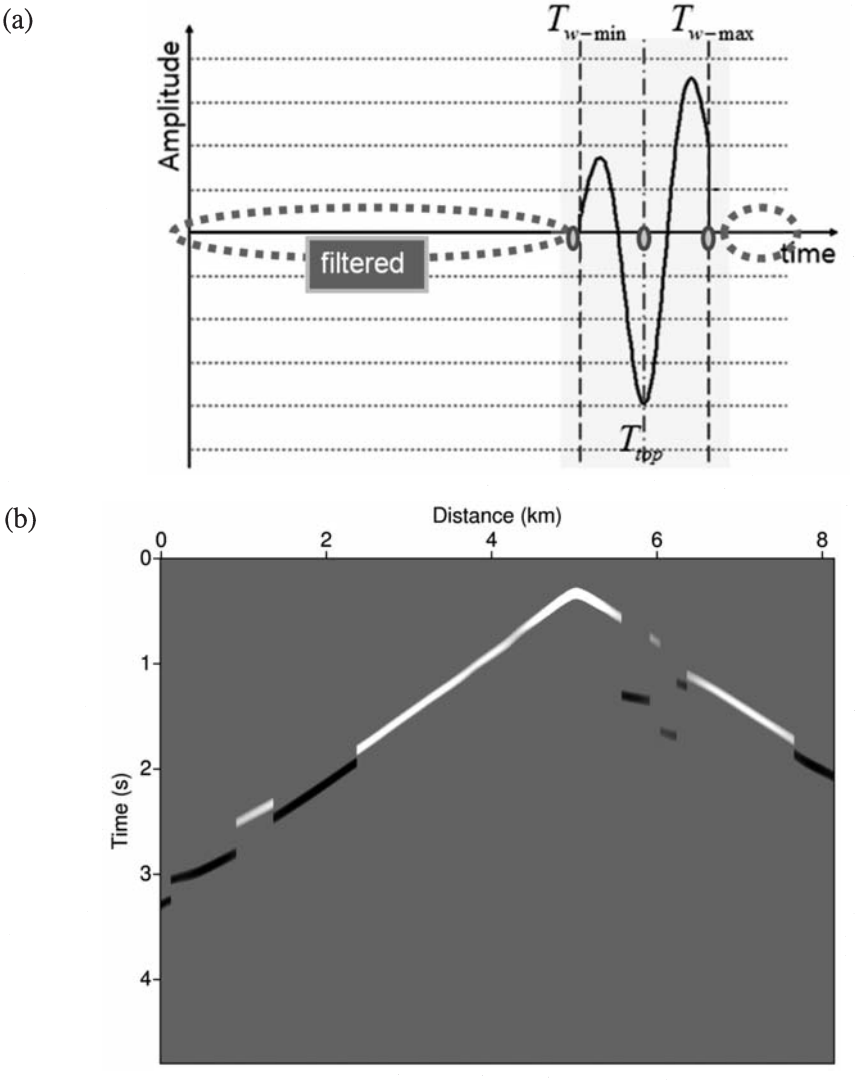

Fig. 4. (a) Data captured by the first time-window; (b) seismogram after the first-time windowing.

NUMERICAL EXAMPLES

Simple anticline model

The proposed algorithm for acoustic time domain full waveform inversion algorithm using the Huber function and time-windows is applied to the simple anticline model, as shown Fig. 7, with a width of 4 km and a depth of 2 km. The observed data is generated via 2D acoustic time domain modeling with the fourth-order finite difference method. We use Higdon's absorbing boundary

condition (Higdon, 1986; Higdon, 1987; Mulder, 1997) and the Dirichlet boundary condition for a free surface (Officer, 1958). The first derivative of Gaussian function with the maximum frequency of 10 Hz is employed as a source wavelet to be estimated with the Green's function. There are 250 shots and receivers; the shot and receiver intervals are both 16 m, and the grid size is the same with the receiver interval. The total recording time is 4.8 s and the sampling interval is 0.0016 s. Information about the model sizes, grid intervals, maximum frequency, total recording time and time interval is given in Table 1.

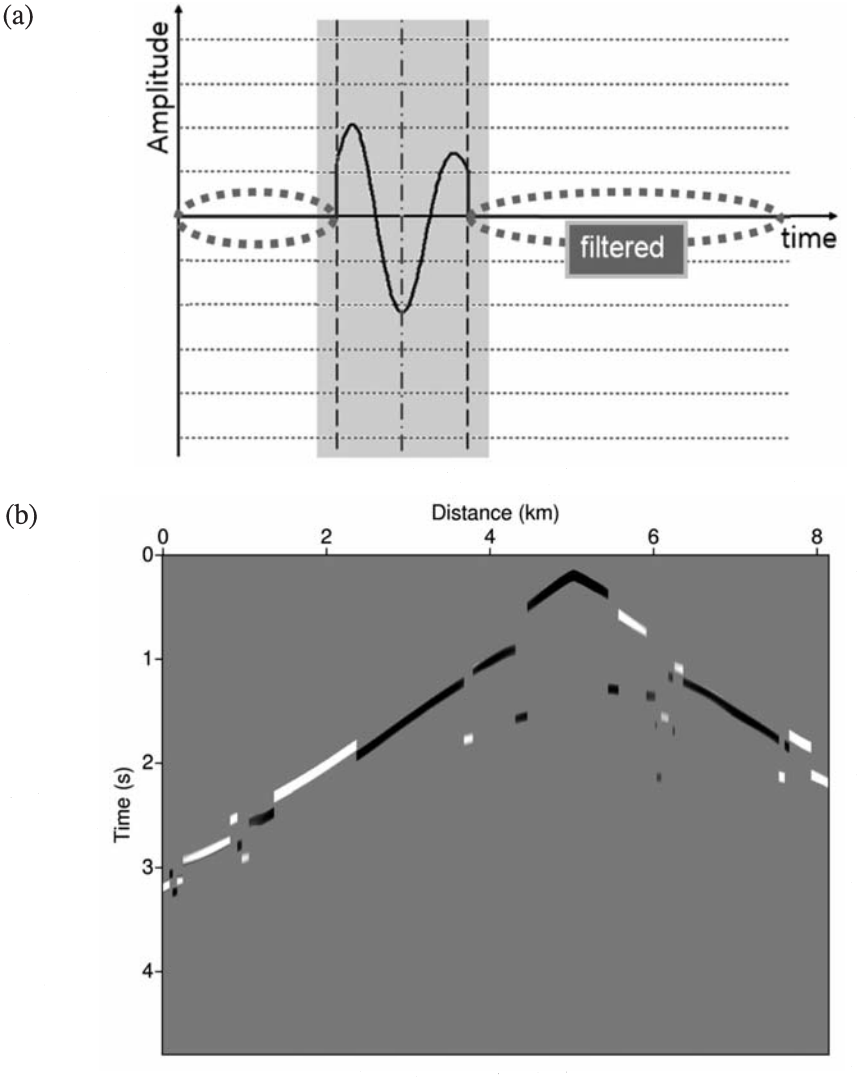

Fig. 5. (a) Data captured by the expanded time-window; (b) seismogram after the expanded time-windowing.

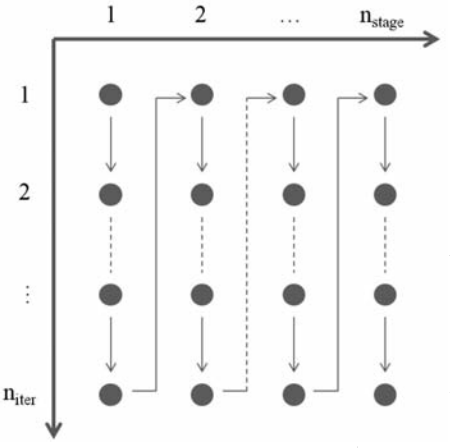

Fig. 6. Diagram of the suggested inversion order.

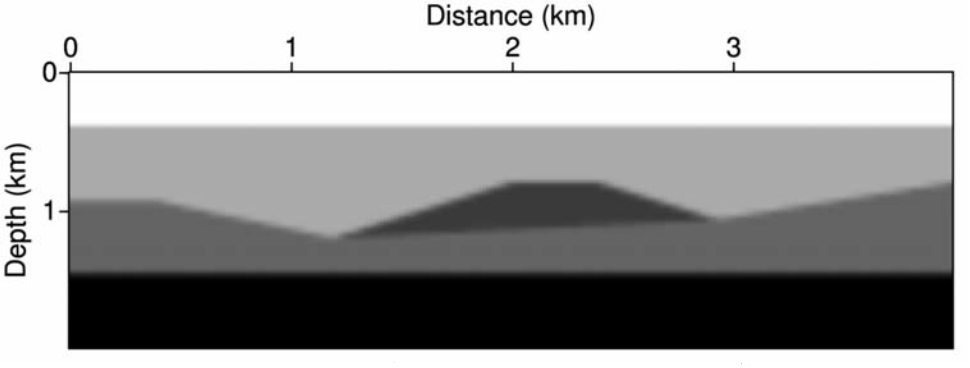

Fig. 7. Simple anticline model.

Table 1. Information on the observed and forward-modeled data of the simple anticline model.

		Observed	Forward-modeled
Model	Size (nx,nz)	(250, 125)	
	Grid interval (m)	16	
Data	The maximum frequency (Hz)	10	estimated
	Total recording time (s)	4,8	
	Time interval (s)	0,0016	

We make q of eq. (19) equal to 0.3, under which one time-window covers 30% of the recording time. The proposed algorithm consists of six stages, including several surplus stages that are employed to avoid the omission of data in the course of the data selection via time-windows. The inner loop of Fig. 6 is iterated 100 times during each stage.

The initial velocity model increased linearly with depth from 1.5 km/s to 3.7 km/s as shown in Fig. 8. Fig. 9(a) shows the result of the first stage of the proposed algorithm, including the inverted velocity obtained by back-propagating the residuals in the first time-window. In Fig. 9(b), the depth profiles that are located 2.24 km from the left edge of the model are shown, where the solid line is the true velocity, the dotted line is the initial velocity, and the dashed line is the inverted velocity. The inverted velocity is close to the true model. This velocity is adopted as the new initial velocity in the beginning of the next stage.

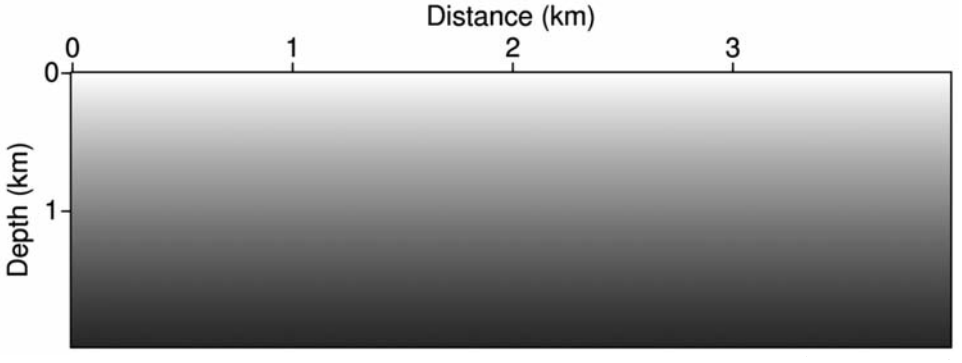

Fig. 8. Initial velocity model for inversion.

As the time-window progresses, data excluded in the time-windows of previous stages are incrementally included through the entire process. Fig. 10 (e) is the final result from the last time-window. The inverted velocity by the proposed algorithm corresponds well with the true velocity in Fig. 10(e). The depth profiles in Fig. 11 confirm that the final result is accurate. In Fig. 11, the depth profiles located 2.24 km from the left edge of the model are shown, where the solid line is the true velocity, the dotted line is the initial velocity, and the dashed line is the inverted velocity. The relative square of the residual, $E(\mathbf{p}_i)/E(\mathbf{p}_1)$, stops decreasing after 600 iterations, as shown in Fig. 12 indicating the proposed algorithm is finished with six partial inversions performed over 100 iterations.

(a)

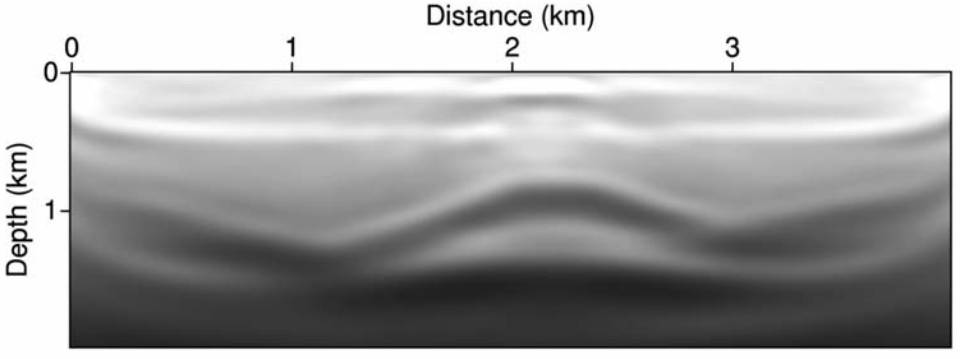

(b)

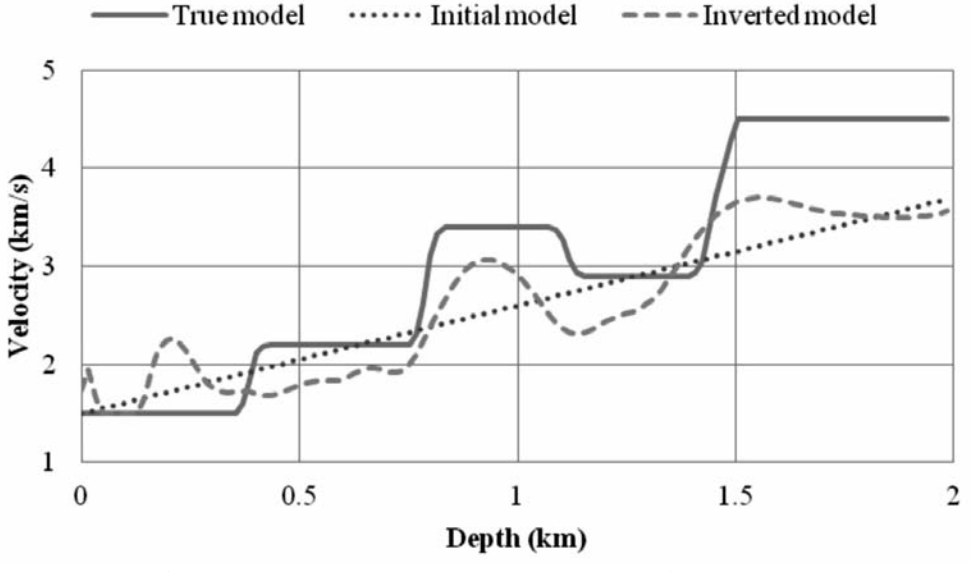

Fig. 9. (a) Inverted velocity after the first time-windowing; (b) profiles of the true, initial and inverted velocities, where the solid line is the true velocity, the dotted line is the initial velocity, and the dashed line is the inverted velocity.

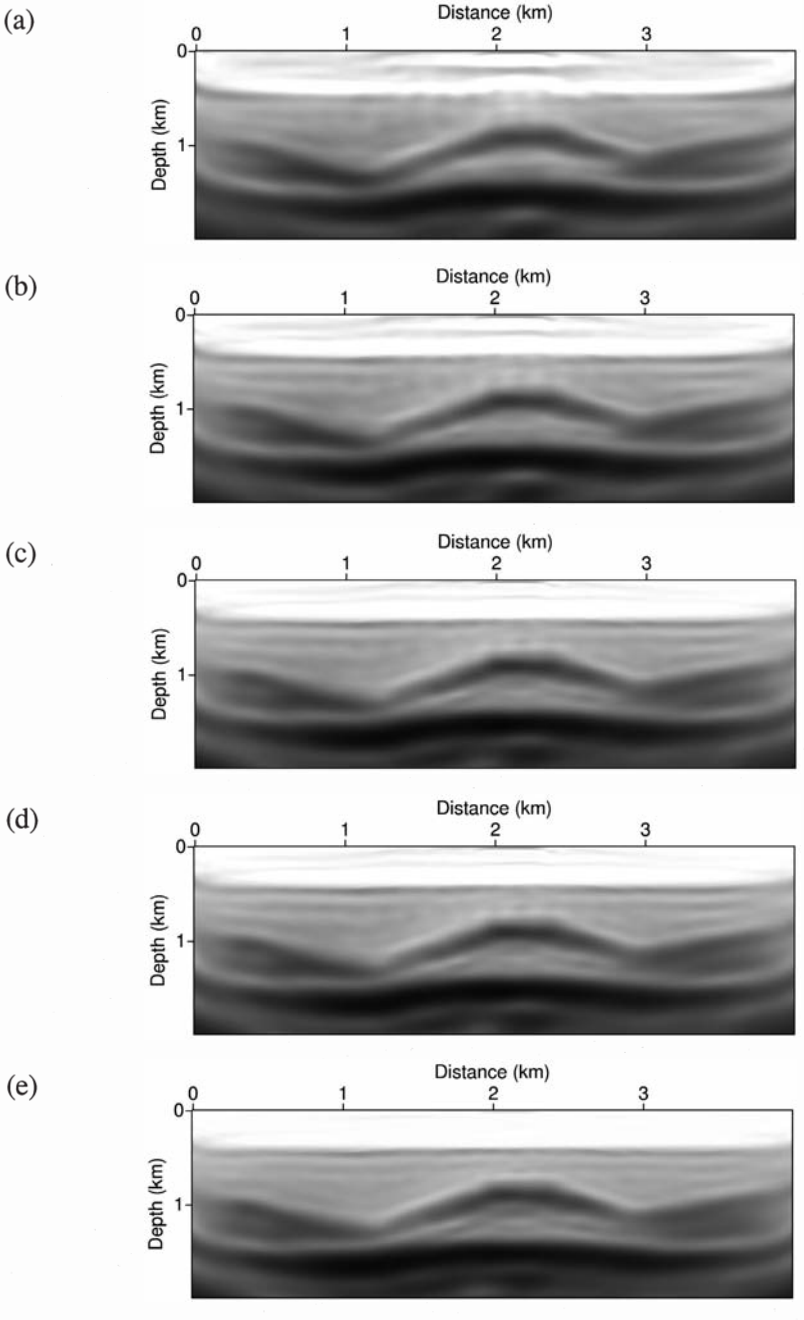

Fig. 10. Inverted velocity of (a) the second, (b) third, (c) fourth, (d) fifth and (e) last stage of the proposed algorithm.

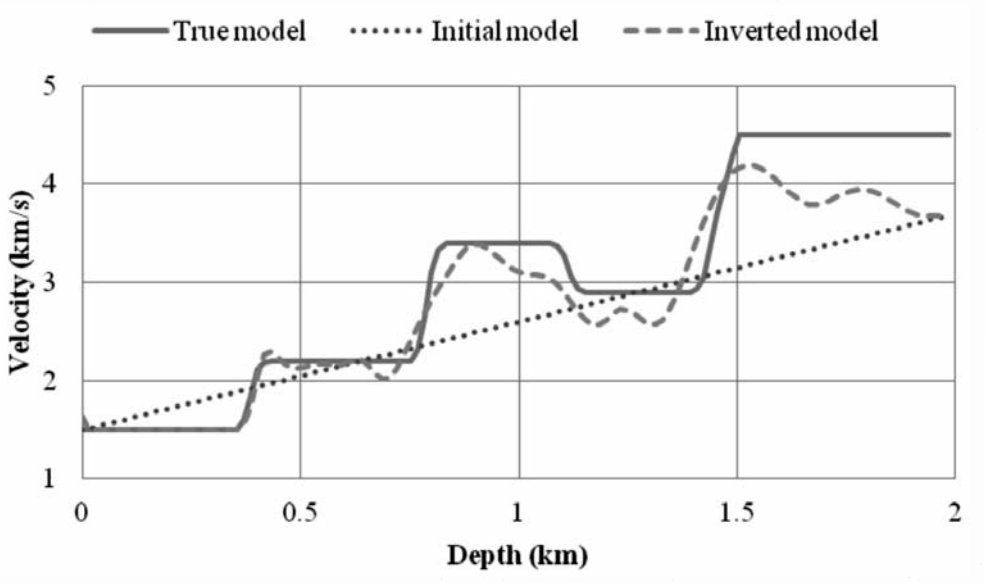

Fig. 11. Profiles of the true, initial and inverted velocities, where the solid line is the true velocity, the dotted line is initial velocity, and the dashed line is the inverted velocity.

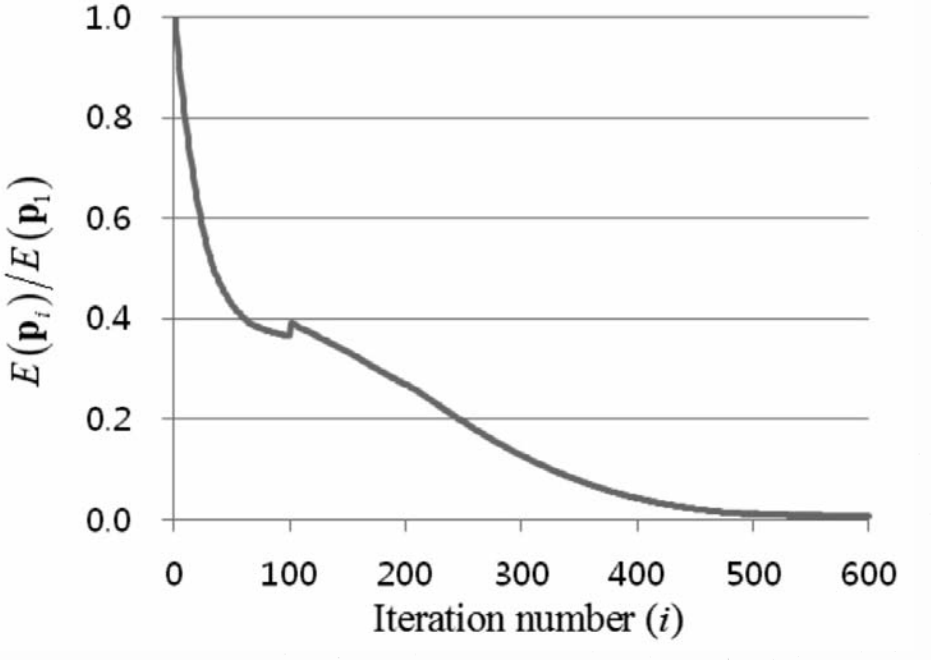

Fig. 12. Error curve of the inversion for the simple anticline model as a function of the number of iteration numbers with updated parameters.

Institut Français du Pétrole Marmousi model

We also investigate the applicability of the proposed algorithm to low-pass filtered observed data from the IFP Marmousi model with a width of 8.16 km and depth of 2.72 km, as shown in Fig. 13. The observed data is generated via 2D acoustic time domain modeling with the fourth-order finite difference method. Higdon's absorbing boundary condition and the Dirichlet boundary condition for a free surface are applied. We excite 509 sources at an interval of 0.016 km and record data at 509 receivers that are spread over the surface. The shot and receiver intervals are 16 m. The total recording time is 4.8 s, and the sampling interval is 0.0016 s. The first derivative of the Gaussian function with the maximum frequency 10.666667 Hz is employed as a source wavelet. The observed data undergo low-pass filtering and interpolation with adjusted grid sizes because different frequencies, grid intervals and model sizes are used to generate the observed and forward-modeled data. In the course of the full waveform inversion, the source wavelet is estimated with the Green's function for inverted velocity model at each step of iterations. Information about the model sizes, grid intervals, maximum frequencies, total recording time, and time interval is provided in Table 2.

Table 2. Information on the observed and forward-modeled data of the IFP Marmousi model.

		Observed	**Forward-modeled**
Model	Size (nx,nz)	(510, 170)	(453, 151)
	Grid interval (m)	16	18
Data	The maximum frequency (Hz)	10.66667	estimated
	Total recording time (s)	4,8	
	Time interval (s)	0,0016	

We define the length of one time-window as that covering approximately 20 % of the entire recording time of the observed data, and the proposed algorithm consists of four stages. Surplus stages are not used in this case because the data not chosen by the four time-windows includes noise resulting from the low-pass filtering. The inner loop of Fig. 6 is iterated 50 times during each stage.

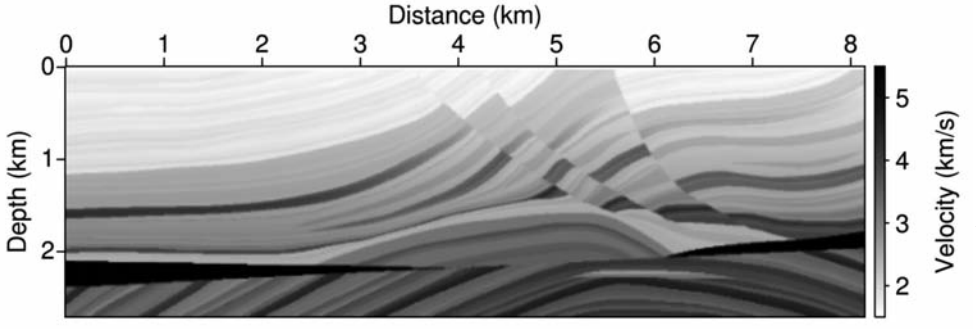

Fig. 13. IFP Marmousi model.

Fig. 14 shows the initial velocity model, which increases linearly with depth from 1.5 km/s to 3.7 km/s. Fig. 15(a) shows the results of the first stage of the proposed algorithm, which provides the inverted velocity obtained by back-propagating the residuals captured by the first time-window. Fig. 15(b) shows the final result after all of the stages set by the number of time-windows are completed. The inverted velocity is close to the true model, although data underwent low-pass filtering. We can confirm that the relative square of the residual as shown in Fig. 16 has a decreasing trend and instant fluctuation with six time-windows each with 150 iterations.

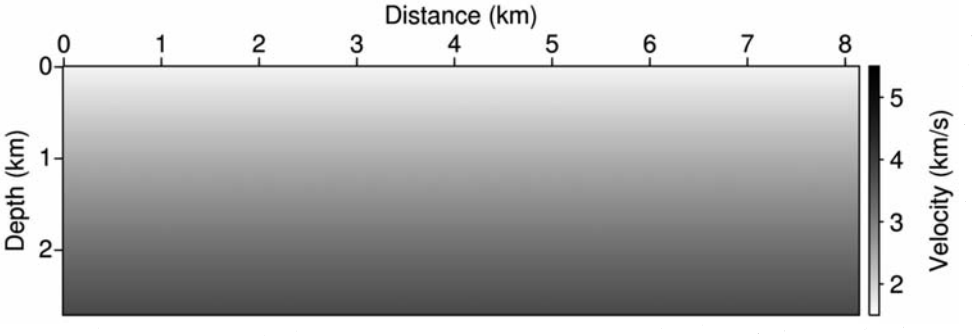

Fig. 14. Initial velocity model.

Real data: Gulf of Mexico

In this section, we apply the proposed algorithm to real data to examine its field applicability. The data are acquired from the Gulf of Mexico. There are

(a)

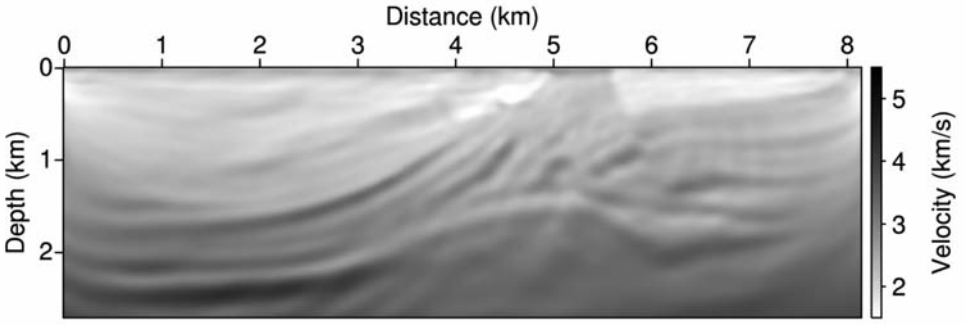

(b)

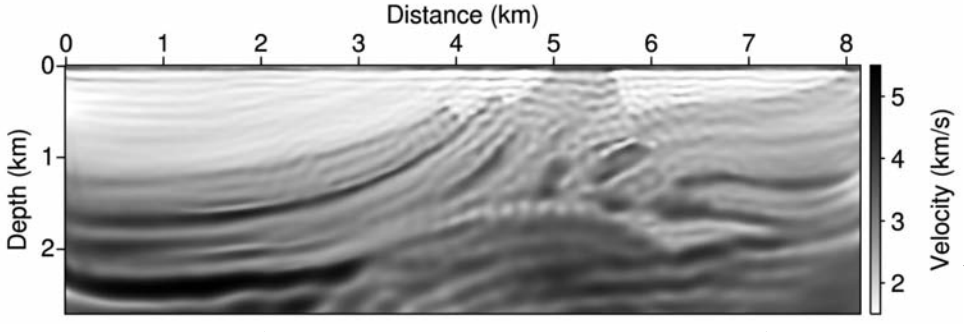

Fig. 15. (a) Inverted velocity using the first time-window; (b) Inverted velocity using the last time-window.

399 shots and 408 channels, and the shot and receiver intervals are 50 m and 25 m, respectively. The offset ranges from 137 m to 10.321 km, and the water depth ranged from 420 m to 910 m. The recording length is 12 s, and the recording time interval is 0.004 s. In the real data case, which does not contain available low-frequency data, we do not perform low-pass filtering. Examples of the common shot gathers are shown in Fig. 17.

We use the observed data recorded from 0 s to 4 s due to computational burdens. To generate the forward-modeled data, we set the grid interval to 20 m and the time interval to 0.002 s. and use Higdon's absorbing boundary condition and the Dirichlet boundary condition for a free surface are applied. During the inversion, the velocity of the sea water layer is constant at 1.5 km/s, and the depth of the sea water is fixed to the values described above. The proposed algorithm consists of four stages and has the inner loop (Fig. 6) of 50 iterations during each stage. Each time-window covers approximately 40% of the total recording time, and four time-windows are employed to avoid the omission of data in the course of the data selection via time-windows.

We use the relative amplitude scaling and residual of eq. (18), and obtain the estimated source wavelet with mutilated amplitudes. This feature causes the residual to be dominated by the observed data, and make inverted result similar to the reverse-time migration images. Fig. 18(b) is the inverted result by the proposed algorithm with the simple starting model shown in Fig. 18(a). This result shows that the velocity could be reconstructed more accurately if a more accurate starting model is used. We employ the velocity model inverted in the Laplace domain (Shin and Cha, 2009) as an initial velocity model, as shown in Fig. 19. Figs. 20 and 21 show the results from the conventional and proposed algorithms, respectively.

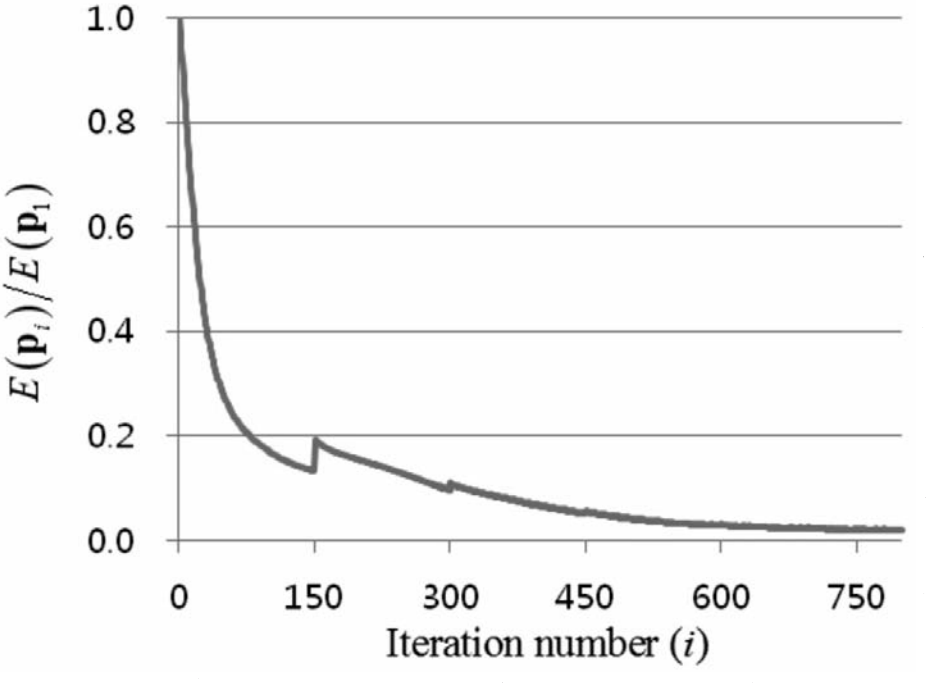

Fig. 16. Error curve of the inversion for the Marmousi model as a function of the number of iterations with updated parameters.

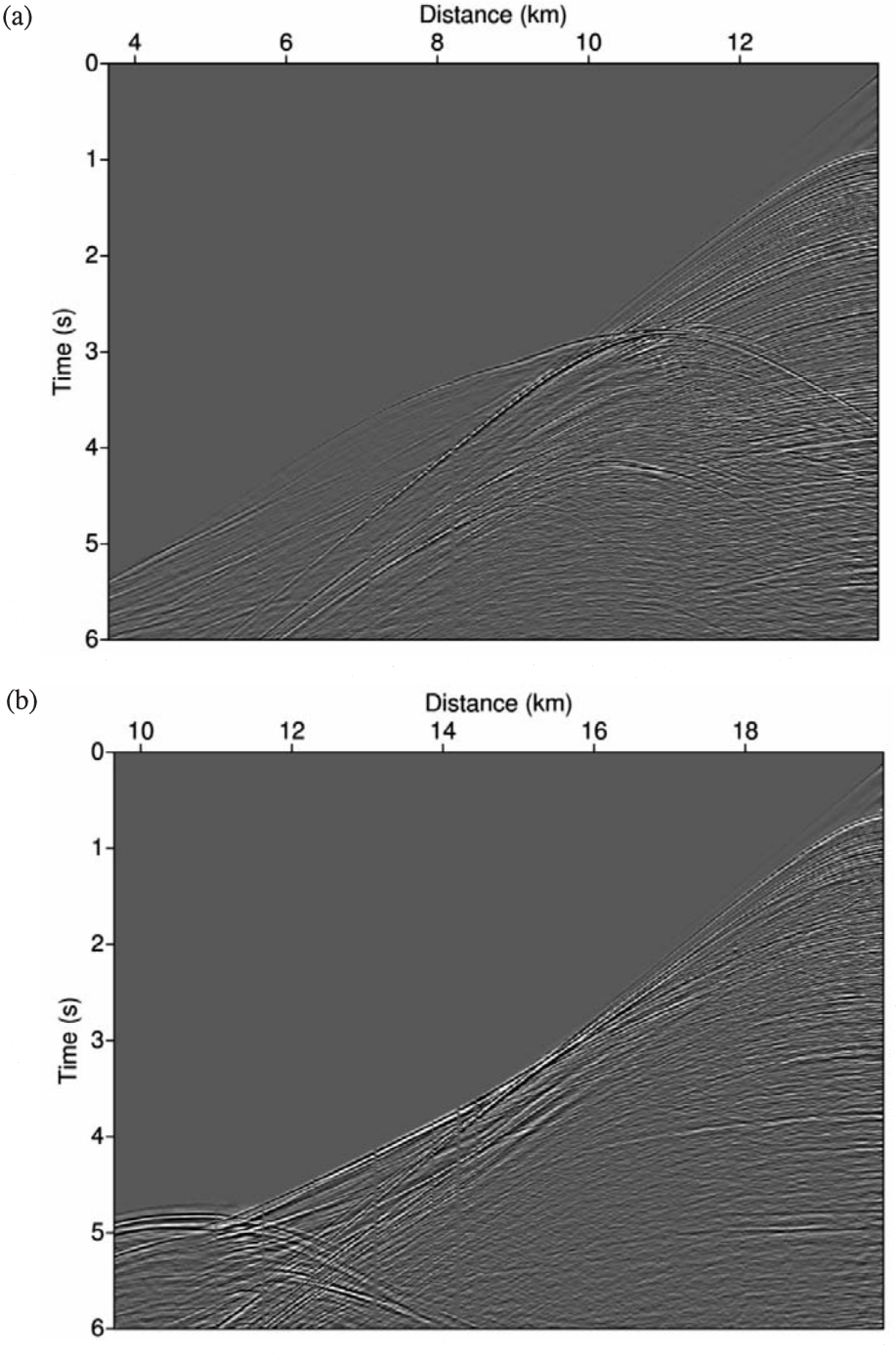

Fig. 17. Common shot gather of (a) the 220th shot and (b) the 340th shot.

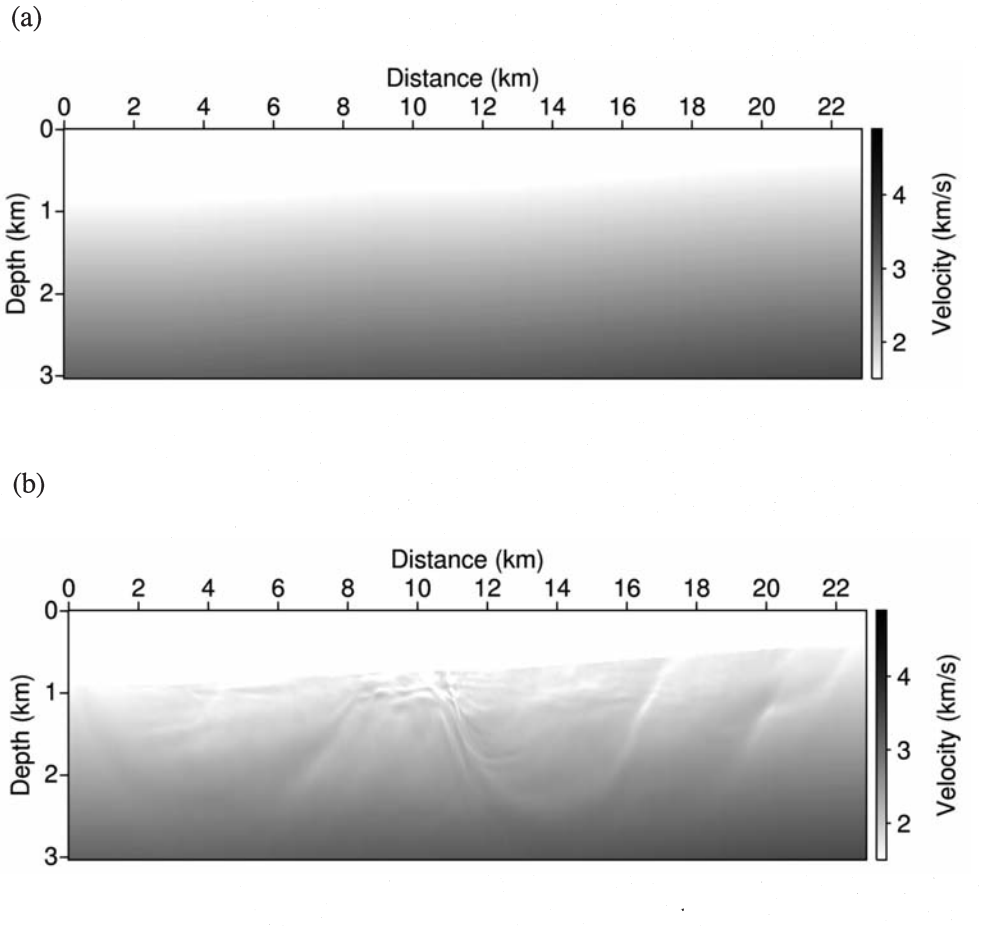

Fig. 18. (a) Initial model, (b) inverted velocity with the proposed algorithm

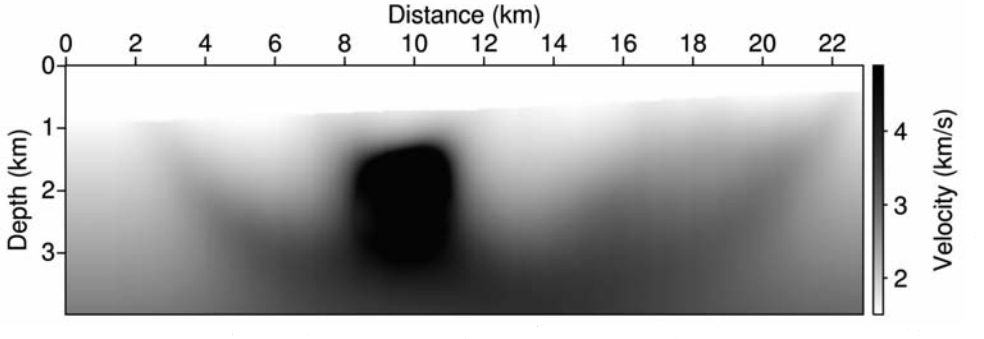

Fig. 19. Initial velocity model from the Laplace domain inversion.

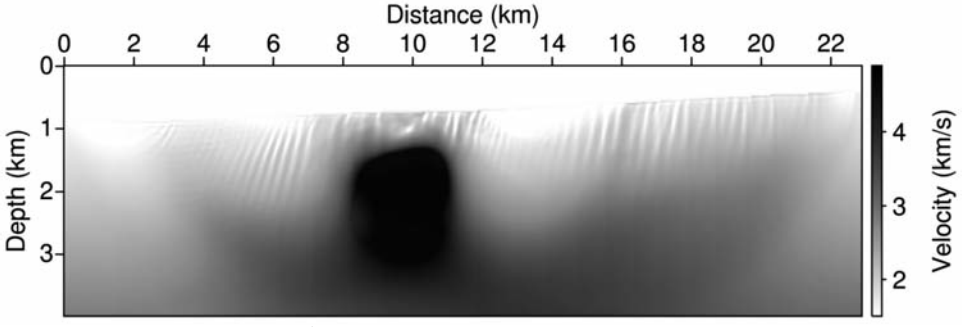

Fig. 20. Inverted velocity model with the conventional algorithm.

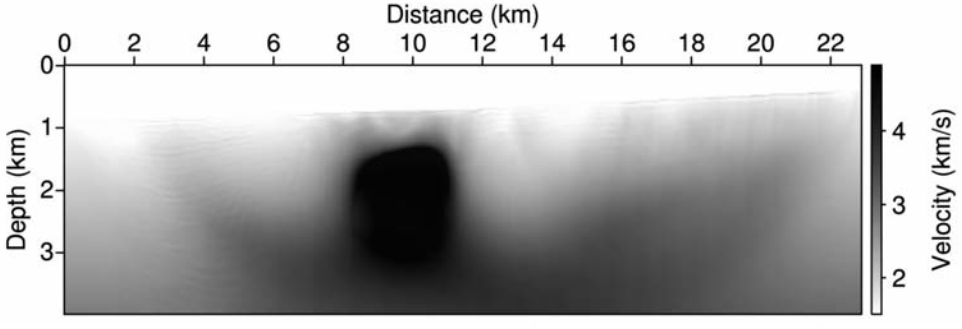

Fig. 21. Inverted velocity model with the proposed algorithm using time-windows.

Fig. 22 shows the relative square of the residual, where the solid line is the error curve from the proposed algorithm, and the dashed line is the error curve from the conventional algorithm. The proposed algorithm for the real data has 4 time-windows with 50 iterations each and has a smaller error curve than the conventional algorithm.

We calculate synthetic seismograms, which is the same procedure with forward modeling of performed full waveform inversion. Seismograms in Fig. 23 are the 220-th common shot gathers. Fig. 23(a) is generated from the inverted velocity model by the conventional full waveform inversion, and Fig. 23(b) is generated from inverted velocity model by the proposed algorithm using time-windows. Compared with the true data shown in Fig. 17, artifacts in the

common shot gathers are more noticeable in Fig. 23(a) than in Fig. 23(b). Seismograms with artifacts including Fig. 23(b) are used in the course of the conventional full waveform inversion. Thus it can be inferred that the artifacts hinder the conventional algorithm in converging to the solutions.

We compare synthetic traces with a trace from the real data. Because the central frequency of the real data is higher than frequency components used in this inversion, a low-pass filter is applied to the real data to attenuate signals with frequencies higher than 5 Hz. Fig. 24 shows traces extracted at 6.2 km from the left edge of the common shot gather for the 220-th shot. In Fig. 24, solid lines represent the filtered real data. The trace with a dashed line in Fig. 24(a) is obtained from the initial velocity model of Fig. 19. It is confirmed that the trace obtained from the initial model is deviated from that extracted from the real data. The trace with a dashed line in Fig. 24(b) is synthesized from the velocity model (shown in Fig. 20) inverted by the conventional algorithm. Fig. 24(b) illustrates that the phase of synthetic trace obtained from conventional inversion technique is deviated from that of the filtered real data. The trace with a dashed line in Fig. 24(c) is obtained from the velocity model of Fig. 21 inverted by our proposed algorithm. Fig. 24(c) shows that the synthetic trace is similar to the trace extracted from the filtered real data.

We perform the reverse-time migration with inverted results. Figs. 25(a) and 25(b) display the migration images obtained from the velocity model of Fig. 20 inverted by the conventional algorithm and from the velocity model of Fig. 21 inverted by the proposed algorithm, respectively. Comparing Fig. 25(b) with

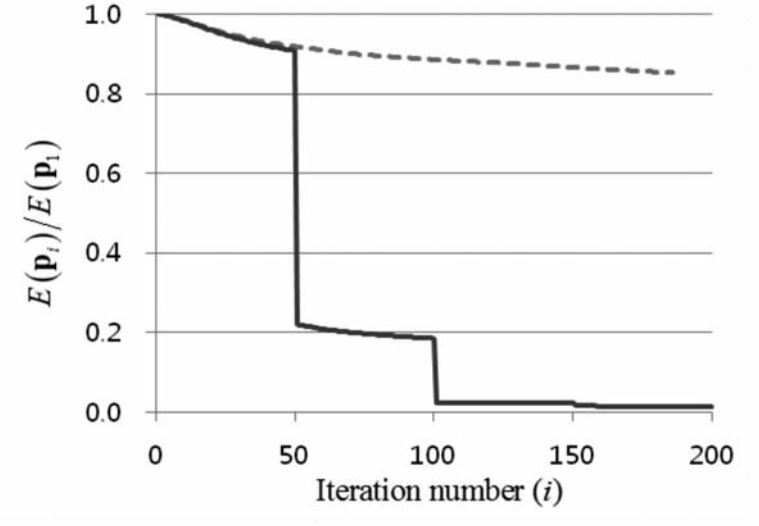

Fig. 22. Error curves of the inversion for the real data in the Gulf of Mexico as a function of the number of iterations with updated parameters: the solid and dashed lines are for the proposed algorithm and conventional algorithm, respectively.

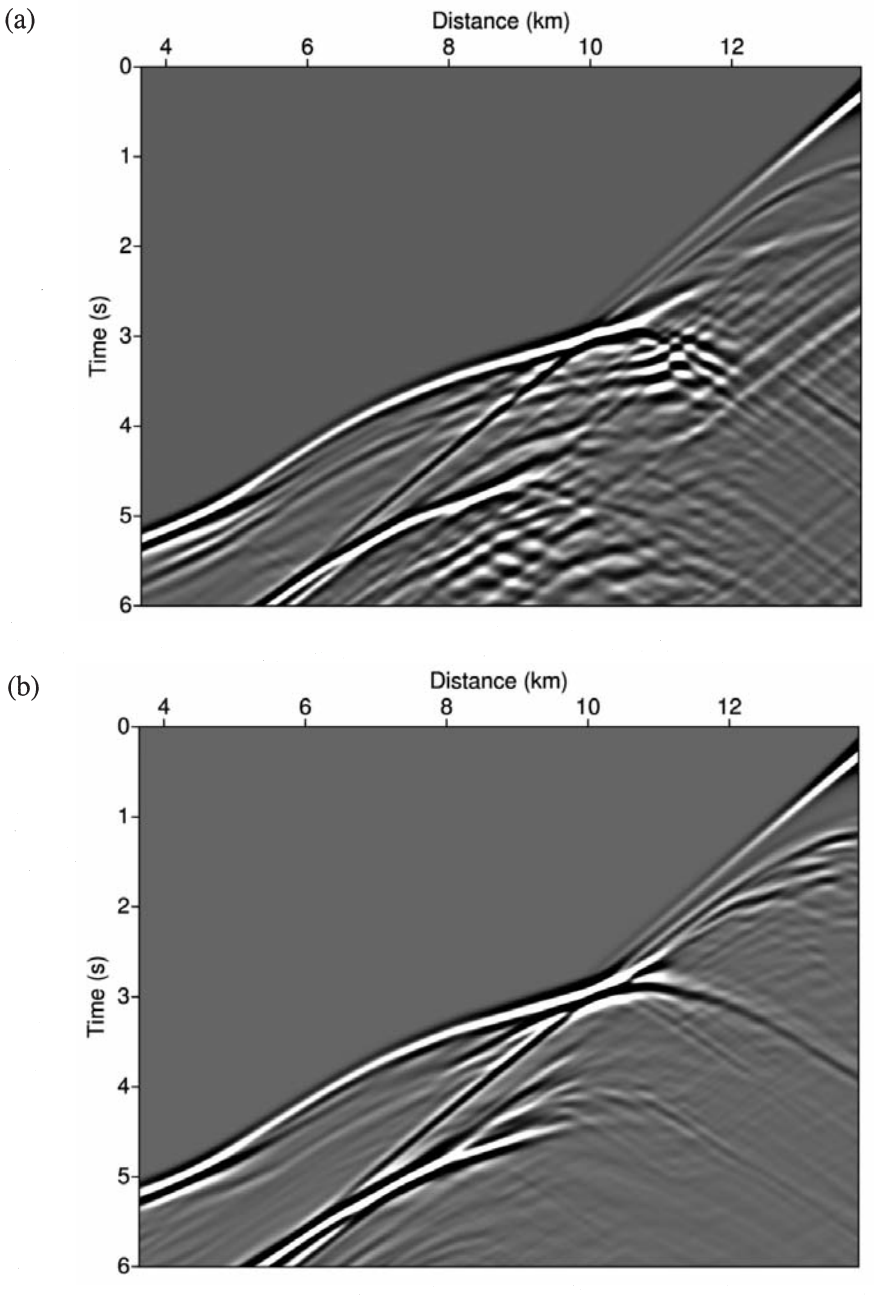

Fig. 23. The 220th common shot gathers from (a) the velocity shown in Fig.20 inverted by the conventional algorithm, and (b) the velocity shown in Fig. 21 by the proposed algorithm.

25(a), we can demonstrate the superiority of the proposed algorithm. In Fig. 25(b), the structures of layers in circles are described distinctly and the better lateral continuity along the entire area is shown. In Fig. 25(a), there are artifacts including adjacent parts indicated by arrows. The velocity model inverted by the conventional algorithm has the upper parts deformed vertically, which would result in these artifacts.

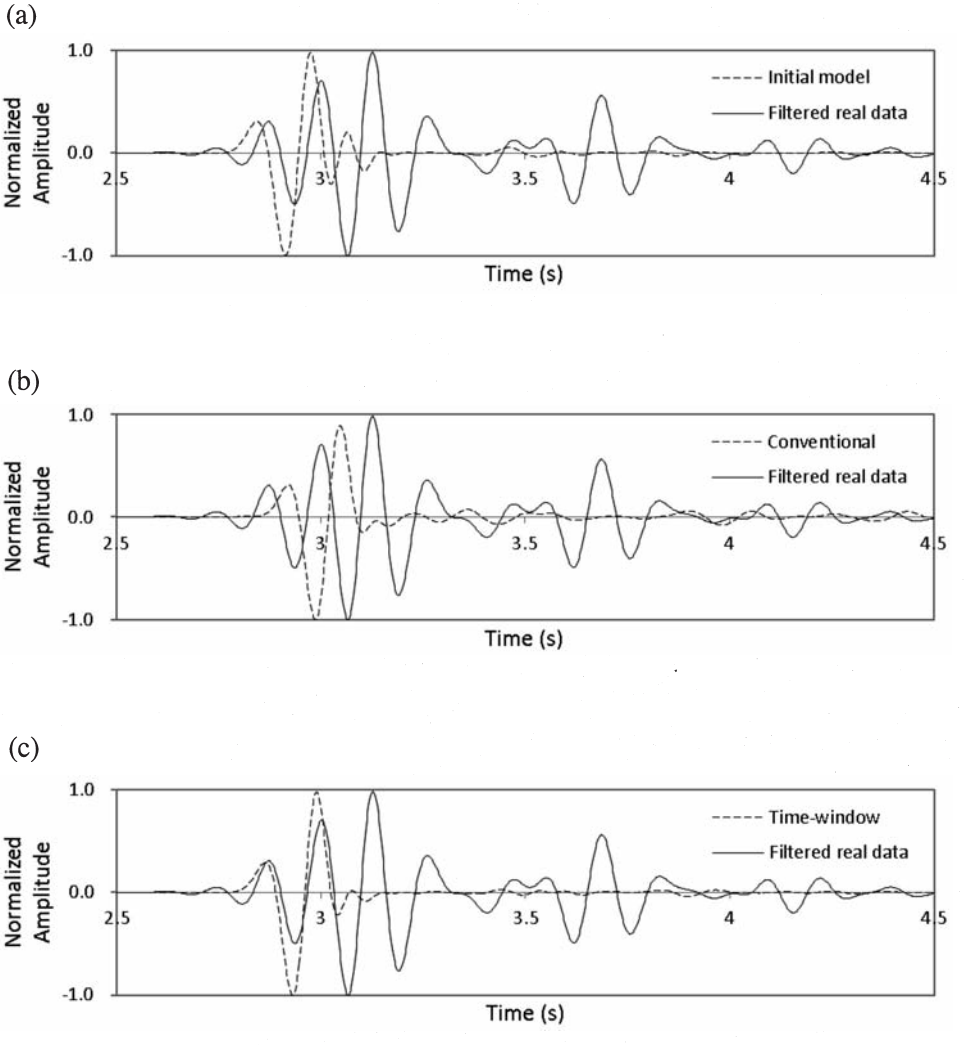

Fig. 24. Traces extracted at 6.2 km from the left edge of the common shot gather for the 220th shot: the solid line represents a trace from the filtered real data, dashed lines of (a), (b), and (c) represent traces calculated from the initial velocity model, the velocity model inverted by the conventional algorithm, and the velocity model inverted by out proposed algorithm.

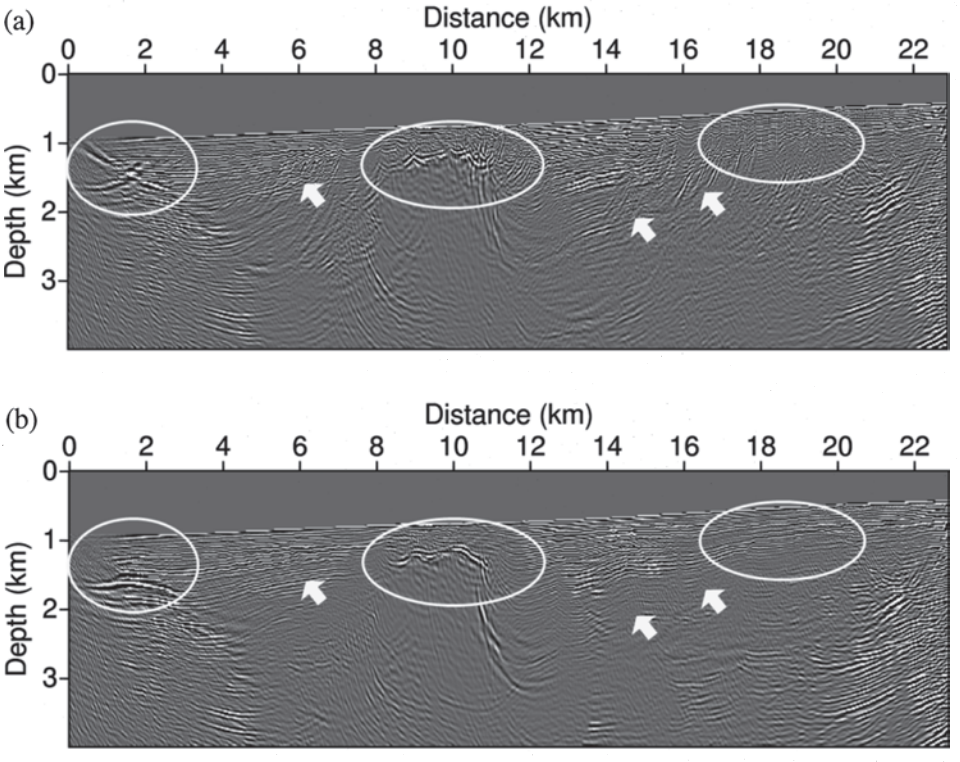

Fig. 25. The reverse-time migration images obtained from (a) the velocity model inverted by the conventional algorithm, and (b) the velocity model inverted by the proposed algorithm as a background model.

CONCLUSION

We performed a full waveform inversion in the time domain with the Huber norm, source estimation and data selection by time-windows. For the full waveform inversion in the time domain, we applied the Huber function and the approximated Hessian matrices, both of which were previously used in the frequency domain. We did not undertake difficult implementation of matrix solver because the full waveform inversion in the time domain does not require solvers in the course of forward modeling. The partial derivative wavefield was calculated with the virtual source vectors. The source wavelet was updated simultaneously by inverting the velocity information. The proposed algorithm was successfully applied to two synthetic examples: data from the simple anticline model and low-pass filtered data from the IFP Marmousi model, and one field data set of real data acquired from the Gulf of Mexico. We confirmed that the inversion results with synthetic datasets correspond well with true models. In the real data example, reasonable inversion results were obtained.

ACKNOWLEDGEMENTS

This work was supported by the Energy Efficiency & Resources (No.2010T100200376) of the Korea Institute of Energy Technology Evaluation and Planning (KETEP), the Basic Research Project (GP2012-040) of the Korea Institute of Geoscience and Mineral Resources (KIGAM), and the Human Resources Development program (No.20124010203200) of KETEP grant funded by the Korean government's Ministry of Knowledge Economy.

REFERENCES

Bourgeois, A., Bourget, M., Lailly, P., Poulet, M., Ricarte, P. and Versteeg, R., 1991. Marmousi, model and data. In: Vesteeg, R. and Grau, G. (Eds.), The Marmousi Experience, Proc. 1990 EAEG Worksh. Pract. Asp. Seism. Data Invers., EAEGS: 5-16.

Bube, K. and Nemeth, T., 2007. Fast line searches for the robust solution of linear systems in the hybrid 1/2 and Huber norms. Geophysics, 72: A13-A17.

Ha. T., Chung, W. and Shin, C., 2009. Waveform inversion using a back-propagation algorithm and a Huber function norm. Geophysics, 74: R15-R24.

Higdon, R.L., 1986. Absorbing boundary conditions for difference approximations to the multidimensional wave equation. Mathemat. Computat., 47: 437-459.

Higdon, R.L., 1987. Numerical absorbing boundary conditions for the wave equation. Mathemat. Computat., 49: 65-90.

Huber, J., 1973. Robust regression: Asymptotics, conjectures and Monte Carlo. Annals Statist., 1: 799-821.

Kim, Y., Cho, H., Min, D.-J. and Shin, C., 2011. Comparison of frequency-selection strategies for 2D frequency-domain acoustic waveform inversion. Pure Appl. Geophys., 10: 1715-1727.

Kim, Y., Min, D.-J. and Shin, C., 2011. Frequency-domain reverse-time migration with source estimation. Geophysics, 76: S41-S49.

Mulder, W.A., 1997. Experiments with Higdon's absorbing boundary conditions for a number of wave equations. Computat. Geosc., 1: 85-108.

Officer, C.B., 1958. Introduction to the Theory of Sound Transmission with Application to the Ocean. McGraw Hill Book Co., Inc., New York.

Pratt, R.G., 1999. Seismic waveform inversion in the frequency domain. Part 1: Theory and verification in a physical scale model. Geophysics, 64: 888-901.

Shin, C., Jang, S. and Min, D.-J., 2001. Improved amplitude preservation for prestack depth migration by inverse scattering theory. Geophys. Prosp., 49: 502-606.

Shin, C. and Min, D.-J., 2006. Waveform inversion using a logarithmic wavefield. Geophysics, 71: R31-R42.

Shin, C., Pyun, S. and Bednar, J.B., 2007. Comparison of waveform inversion. Part 1: Conventional wavefield vs. logarithmic wavefield. Geophys. Prosp., 55: 449-464.

Shin, C. and Cha, Y.H., 2009. Waveform inversion in the Laplace-Fourier domain. Geophys. J. Internat., 177: 1067-1079.

Sirgue, L. and Pratt, R.G., 2004. Efficient waveform inversion and imaging. A strategy for selecting temporal frequencies. Geophysics, 69: 231-248.

Song, Z.-M. and Singh, S.C., 2002. Two-dimensional full wavefield inversion of wide-aperture marine seismic streamer data. Geophys. J. Internat., 151: 325-344.

Tarantola, A., 1984. Inversion of seismic reflection data in the acoustic approximation. Geophysics, 49: 1259-1266.

Varela, C.L., Stoffa, P.L. and Sen, M.K., 1998. Background velocity estimation using non-linear optimization for reflection tomography and migration misfit. Geophys. Prosp., 46: 51-78.

Vigh, D. and Starr, E.W., 2008. 3D prestack plane-wave, full-waveform inversion. Geophysics, 73: VE135-VE144.